THE UNIVERSITY of EDINBURGH

Edinburgh Research Explorer

Gravity-driven flow of Herschel--Bulkley fluid in a fracture and in a 2D porous medium

OPEN ACCESS

Gravity-driven flow of Herschel–Bulkley fluid in a fracture and in a 2D porous medium

V. Di Federico[1], S. Longo[2], S. E. King[3], L. Chiapponi[2], D. Petrolo[2], V. Ciriello[1]

[1] Dipartimento di Ingegneria Civile, Chimica, Ambientale e dei Materiali (DICAM), Università di Bologna, Viale Risorgimento, 2, 40136 Bologna, Italy

[2]Dipartimento di Ingegneria e Architettura (DIA), Università di Parma, Parco Area delle Scienze, 181/A, 43124 Parma, Italy

[3]School of Mathematics, University of Edinburgh, Edinburgh, EH9 3FD, Scotland

(Received)

New analytical models are introduced to describe the motion of a Herschel–Bulkley fluid slumping under gravity in a narrow fracture and in a porous medium. A useful self–similar solution can be derived for a fluid injection rate that scales as t; an expansion technique is adopted for a generic injection rate which is power–law in time. Experiments in a Hele–Shaw cell and in a narrow channel filled with glass ballotini confirm the theoretical model within the experimental uncertainty.

Key words: gravity currents, Herschel–Bulkley fluid flows, porous media

1. Introduction

Implications of fluid rheology on flow in fractures and porous media have been extensively analysed in the last years. Artificial fluids and foams are designed to fulfill specific requirements related to aquifer remediation, fracking technology, and soil reinforcing. In some conditions, Carbon Dioxide stored in aquifers may behave as a non–Newtonian fluid (Wang & Clarens 2012). Darcy's law, valid for Newtonian fluids, has been extended, with various methodologies, to power–law non–Newtonian fluids and experimentally validated; see Cristopher & Middleman (1965), Barletta & de B. Alves (2014) and references therein.

Viscous gravity currents of power–law (Ostwald–de Waele, Ostwald 1929) fluids in wide channels and in fractures have been extensively investigated, formulating specific models for various geometrical configurations and providing an experimental verification. Gratton *et al.* (1999) and Perazzo & Gratton (2005) presented a comprehensive theoretical framework for unidirectional and axisymmetric flow over a horizontal plane and down an incline. Longo *et al.* (2013*a*) investigated experimentally horizontal spreading in radial geometry, while Longo *et al.* (2015*c*) and Longo *et al.* (2015*d*) examined the advance in horizontal and inclined channels, taking into account the shape of the cross section, and longitudinal variations of cross section and bottom inclination.

Gravity currents of a power–law fluid in porous media have recently been analysed with a combination of analytical, numerical, and experimental techniques (e.g., Longo *et al.* 2013*b*; Di Federico *et al.* 2014; Longo *et al.* 2015*a*; Ciriello *et al.* 2016).

However, even though the power–law approximation provides an accurate interpretation of fluid behaviour in several flow conditions, it does not cover other classes of fluids

exhibiting yield stress. These are better described by models such as Herschel–Bulkley (three parameters, Herschel & Bulkley 1926), Cross (four parameters, Cross 1965), and Carreau-Yasuda (four or five parameters, Carreau 1972; Yasuda *et al.* 1981).

Gravity currents of Herschel–Bulkley fluids (HB) on horizontal and inclined planes, or in wide channels, have been analysed theoretically and experimentally by several authors. Hogg & Matson (2009) modelled two-dimensional currents, focusing their attention on the front geometry, its role in the overall dynamics, and the arrested state for a dam-break process. Huang & Garcia (1998), Vola *et al.* (2004), and Balmforth *et al.* (2006) investigated the propagation numerically. Further experimental contributions were provided by Ancey & Cochard (2009) in dam-break configuration, and by Chambon *et al.* (2014) in steady uniform regime. The special case of Bingham fluids was analysed by Liu & Mei (1989); the effect of finite-width channels was explored by Mei & Yuhi (2001) and Cantelli (2009). A recent review (Coussot 2014) critically lists the numerous papers on flows of HB fluids in several geometries and conditions. The effect of a realistic channel geometry mimicking natural channelized flow was analysed in Longo *et al.* (2016), where a HB fluid was injected with a constant discharge rate in a channel widening and reducing its bottom inclination downstream.

As to porous flow of yield stress fluids, a key element is the reliability of the model relating flow rate and pressure gradient. According to Chevalier *et al.* (2013), porous flow of an Herschel–Bulkley fluid is characterised by multiple length scales, and at least one of them is not related to the geometry of the pores and connecting channels, but depends on the pressure drop. Hence, the flow starts along specific, limited paths near the threshold pressure drop. Subsequently the sequence of converging and diverging throats encountered by the fluid facilitates a progressive increment of the mobilized fluid domain as the pressure drop increases, rather than a sharp increase in the extent of mobilized fluid. Further experiments (Chevalier *et al.* 2014) have demonstrated that the domain of fluid at rest is very limited even for very low velocity. This complex behaviour increases the difficulties in modeling yield stress fluids, and strengthens the need to verify existing formulations of the flow law valid at Darcy's scale with carefully conducted experiments.

The existing body of knowledge on HB flows, accumulated mostly in recent years, leaves open several avenues of investigation. To the best of our knowledge, the behaviour of HB fluids flowing in a narrow channel (a fracture) has not been investigated to the same extent as flows in wide channels, and deserves a more in-depth analysis due to the numerous practical applications of the process, such as polymer processing, heavy oil flow, gel cleanup in propped fractures, drilling processes. In addition, the flow of HB fluids in a porous medium still requires experimental validations to enable extending the results obtained in viscometric flows to more realistic configurations. The present theoretical approach aims to contribute to these aspects, with the crucial support of laboratory experiments.

In this paper we present a theoretical model and its experimental validation for 2D flows of a Herschel–Bulkley fluid in a narrow fracture and in a porous medium. The theoretical model is general, while computations and experiments refer mainly to a specific situation (the injected volume quadratic in time) where a simple self–similar solution is available. An expansion method has been applied to handle, with some restrictions, the general case of an injected volume which is power-law over time; the general method has likewise been experimentally validated.

The paper is structured as follows. Section 2 presents the model for HB flow in a narrow fracture. The self–similar solution is illustrated in Section 3. Flow in a homogeneous porous medium is examined in section 4. Section 5 describes the experiments conducted in a Hele–Shaw cell and in an artificial 2D porous medium. The last section contains the
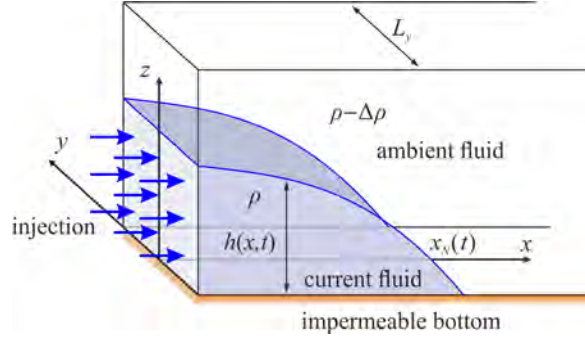
FIGURE 1. Diagram showing the setup of axes and fluid orientation in flow through a narrow fracture (Hele–Shaw cell).

conclusions. Details on rheometry of the yield stress fluids employed in the experiments are included in the Appendix.

2. Model description for flow in a narrow fracture

The HB model for a shear thinning/thickening fluid with yield stress is

$$\begin{cases} \tau &= \left(\mu_0 \dot{\gamma}^{n-1} + \tau_p \dot{\gamma}^{-1} \right) \dot{\gamma}, & \tau \geqslant \tau_p, \\ \dot{\gamma} &= 0, & \tau < \tau_p, \end{cases} \tag{2.1}$$

given in terms of the stress τ and of the strain rate $\dot{\gamma}$. A slightly more complicated description using tensor invariants is required for three dimensional flows; this formulation is not reported here as we consider a one–dimensional problem below. The parameter μ_0, the consistency index, represents a viscosity–like parameter, whilst τ_p is the yield stress of the fluid, and n, the fluid behaviour index, controls the extent of shear–thinning ($n < 1$) or shear–thickening ($n > 1$); $n = 1$ corresponds to the Bingham case. For flow through a narrow fracture (such as a Hele–Shaw cell) of width L_y, as depicted in Figure 1, the primary balance is between cross gap quantities. The relevant relationship is that the velocity $u(x, y)$ in the x–direction must satisfy

$$\begin{cases} \tau_{xy} &= \left(\mu_0 \left| \dfrac{\partial u}{\partial y} \right|^{n-1} + \tau_p \left| \dfrac{\partial u}{\partial y} \right|^{-1} \right) \dfrac{\partial u}{\partial y}, & \tau_{xy} \geqslant \tau_p, \\ \dfrac{\partial u}{\partial y} &= 0, & \tau_{xy} < \tau_p, \end{cases} \tag{2.2}$$

where τ_{xy} represents the cross gap stress and y is the cross gap direction. Furthermore, the primary balance between cross–gap stress and along–fracture pressure gradient is related by $y(\partial p/\partial x) = \tau_{xy}$. We define the height $h(x,t)$ of fluid above a horizontal impermeable base. Then under the relevant shallow water approximation, pressure is to leading order hydrostatic, and the pressure gradient becomes $\partial p/\partial x = \Delta \rho\, g\,(\partial h/\partial x)$, where $\Delta \rho$ is the density difference driving the flow, between fluid within and that outside the gravity current and g acceleration due to gravity. We assume that wetting characteristics at the walls of the fracture are unimportant (or alternately the flow takes place in a pre–wetted fracture). Combining these equations, using the condition that $\tau_{xy} = \tau_p$ as the fluid yields, leads to an expression for the location of the yield surface in the gap, $|y_{yield}| = \tau_p/(\Delta \rho\, g|\partial h/\partial x|)$, where $-L_y/2 \leqslant y_{yield} \leqslant L_y/2$ is required.

To continue, we need to solve for the cross–gap flow structure in yielded and un-yielded

regions of the flow. The continuity of mass of the fluid layer may be written as

$$\frac{\partial h}{\partial t} = -\frac{\partial}{\partial x}\left(\bar{u}h\right),\tag{2.3}$$

where $\bar{u}(x,t)$ is the gap–averaged velocity. Assuming a zero slip velocity, and upon introducing the expression of $\bar{u}(x,t)$ in equation (2.3), we can form an evolution equation for $h(x,t)$ alone, namely

$$\frac{\partial h}{\partial t} = \left(\frac{L_y}{2}\right)^{(n+1)/n}\operatorname{sgn}\left(\frac{\partial h}{\partial x}\right)\left(\frac{n}{2n+1}\right)\left(\frac{\Delta\rho\,g}{\mu_0}\right)^{1/n}\times$$
$$\frac{\partial}{\partial x}\left[h\left|\frac{\partial h}{\partial x}\right|^{1/n}\left(1-\kappa\left|\frac{\partial h}{\partial x}\right|^{-1}\right)^{(n+1)/n}\left(1+\left(\frac{n}{n+1}\right)\kappa\left|\frac{\partial h}{\partial x}\right|^{-1}\right)\right],\tag{2.4}$$

where $\kappa = 2\tau_p/(\Delta\rho\,gL_y)$ is a non dimensional number representing the ratio between yield stress and gravity related stress, or the ratio between the Bingham and the Ramberg number. Additionally setting

$$\Omega = \left(\frac{L_y}{2}\right)^{(n+1)/n}\left(\frac{n}{2n+1}\right)\left(\frac{\Delta\rho\,g}{\mu_0}\right)^{1/n},\tag{2.5}$$

where Ω is a velocity scale, allows us to write this equation slightly more succinctly as

$$\frac{\partial h}{\partial t} =$$
$$\operatorname{sgn}\left(\frac{\partial h}{\partial x}\right)\Omega\frac{\partial}{\partial x}\left[h\left|\frac{\partial h}{\partial x}\right|^{\frac{1}{n}}\left(1-\kappa\left|\frac{\partial h}{\partial x}\right|^{-1}\right)^{\frac{n+1}{n}}\left(1+\left(\frac{n}{n+1}\right)\kappa\left|\frac{\partial h}{\partial x}\right|^{-1}\right)\right].\tag{2.6}$$

To this equation we must add the further condition that when the flow is fully plugged (that is $y_{yield} = L_y/2$) then the velocity throughout the gap is zero ($\bar{u}=0$), so therefore $\partial h/\partial t = 0$ for such regions. This is the limiting version of the equation above in the limit $\partial h/\partial x = \kappa$, which is in turn the condition for the flow to be fully plugged. Consequently, the equation for the height of the current is continuous through such a plugging transition.

In the model, the slip contribution was neglected also because most experiments were conducted by roughening the Hele–Shaw cell with commercial transparent anti slip tape, which is commonly adopted to make slippery surfaces safe. Independent rheometric measurements were conducted with plates roughened with sand paper.

3. Self–similar solution

Various self–similar solutions exist to describe the spreading of gravity currents of constant or variable volume in cases similar to our problem where $\kappa = 0$, $n = 1$ (e.g., King & Woods 2003; Lyle *et al.* 2005), and where $\kappa = 0$ (Pascal & Pascal 1993; Longo *et al.* 2013*b*, 2015*b*; Ciriello *et al.* 2016). For the current study where both yield stress and shear thinning/thickening effects are present, a generalized form of such solutions is not available since the presence of yield stress breaks self–similarity. However, one form of self–similar solution does exist if we allow a variable injection rate of fluid (a more general type of solution with self–similarity of the second kind might be possible, although not attempted here). To this end, suppose that the volume of fluid in the gravity current

varies as

$$L_y \int_0^\infty h(x,t)\mathrm{d}x = Qt^\alpha, \tag{3.1}$$

where $\alpha, Q \geqslant 0$. Then the principal dimensions of the three parameters are $[\Omega] = L/T$, $[Q/L_y] = L^2/T^\alpha$, $[\kappa] = 1$. It is possible to rewrite our principle variables in dimensionless form as

$$\widetilde{h} = h\left(\frac{Q}{L_y\Omega^\alpha}\right)^{1/(\alpha-2)}, \quad \widetilde{x} = x\left(\frac{Q}{L_y\Omega^\alpha}\right)^{1/(\alpha-2)}, \quad \widetilde{t} = t\left(\frac{Q}{L_y\Omega^2}\right)^{1/(\alpha-2)}. \tag{3.2}$$

Introducing these variables immediately reduces equations (2.6–3.1) to the dimensionless form

$$\frac{\partial \widetilde{h}}{\partial \widetilde{t}} = -\frac{\partial}{\partial \widetilde{x}}\left[\widetilde{h}\left|\frac{\partial \widetilde{h}}{\partial \widetilde{x}}\right|^{\frac{1}{n}}\left(1 - \kappa\left|\frac{\partial \widetilde{h}}{\partial \widetilde{x}}\right|^{-1}\right)^{\frac{n+1}{n}}\left(1 + \left(\frac{n}{n+1}\right)\kappa\left|\frac{\partial \widetilde{h}}{\partial \widetilde{x}}\right|^{-1}\right)\right], \tag{3.3}$$

$$\int_0^\infty \widetilde{h}\,\mathrm{d}\widetilde{x} = \widetilde{t}^\alpha, \tag{3.4}$$

where we have assumed that $\partial \widetilde{h}/\partial \widetilde{x} < 0$. Hereafter the tilde is dropped. We can seek self–similar solutions of these equations by looking for solutions in the form $h = t^\beta f(\eta)$ where $\eta = x/t^\gamma$. Substituting into equation (3.3–3.4) yields

$$\beta t^{\beta-1}f - t^{\beta-1}\gamma\eta f' = -\left[t^{\beta+(\beta-\gamma)/n}f|f'|^{\frac{1}{n}}\left(1 - \frac{\kappa t^{\gamma-\beta}}{|f'|}\right)^{\frac{n+1}{n}}\right.$$
$$\left. \times \left(1 + \left(\frac{n}{n+1}\right)\frac{\kappa t^{\gamma-\beta}}{|f'|}\right)\right]' t^{-\gamma}, \tag{3.5}$$

$$\int_0^{\eta_e} t^{\beta+\gamma}f(\eta)\mathrm{d}\eta = t^\alpha, \tag{3.6}$$

where primes denote differentiation with respect to η. Comparing powers of t gives immediately $\beta+\gamma = \alpha$, $\gamma-\beta = 0$, $\beta-1 = (\beta-\gamma)(1+1/n)$. This has one consistent solution, namely $\alpha = 2$ and $\beta = \gamma = 1$. A fluid injection rate scaling as t allows a self–similar solution, for which both the height and length of the current increase with time, similarly scaling as t. However, for $\alpha = 2$ the scales in equation (3.2) break down and an additional velocity scale embedded in the integral constraint of mass conservation given by equation (3.1) arises beyond Ω, given by $(Q/L_y)^{1/2}$. A similar case is treated in Di Federico *et al.* (2012a,b). We define an arbitrary time scale t^*, the velocity scale $u^* = (Q/L_y)^{1/2}$ and the ratio between the two velocity scales $\delta = (L_y\Omega^2/Q)^{1/2}$, with $x^* = u^*t^*$. Equations (3.3–3.4) become

$$\frac{\partial h}{\partial t} = -\delta\frac{\partial}{\partial x}\left[h\left|\frac{\partial h}{\partial x}\right|^{\frac{1}{n}}\left(1 - \kappa\left|\frac{\partial h}{\partial x}\right|^{-1}\right)^{\frac{n+1}{n}}\left(1 + \left(\frac{n}{n+1}\right)\kappa\left|\frac{\partial h}{\partial x}\right|^{-1}\right)\right], \tag{3.7}$$

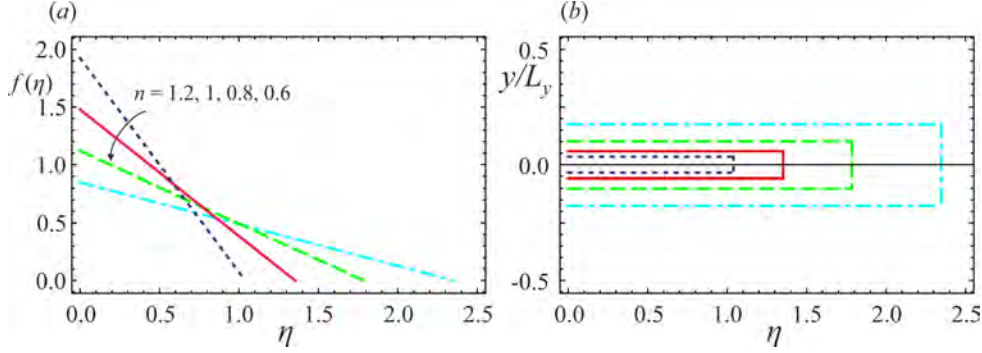$$\int_0^\infty h(x,t)\,\mathrm{d}x = t^2. \tag{3.8}$$

FIGURE 2. (*a*) Shape of the similarity solution in a Hele–Shaw cell ($\alpha = 2$) for different values of n; (*b*) plug regions.

We seek a self–similar solution of the form $h = tf(\eta)$, where $\eta = x/t$; substituting into equations (3.7–3.8) yields

$$f - \eta f' = -\delta \left[f |f'|^{\frac{1}{n}} \left(1 - \frac{\kappa}{|f'|} \right)^{\frac{n+1}{n}} \left(1 + \left(\frac{n}{n+1} \right) \frac{\kappa}{|f'|} \right) \right]', \tag{3.9}$$

$$\int_0^{\eta_e} f(\eta) \, d\eta = 1. \tag{3.10}$$

This system admits a simple solution, namely a linear profile for $f(\eta)$ (Di Federico *et al.* 2012*a*). Supposing a solution in the form $f(\eta) = A(\eta_e - \eta)$, for some constants $A > 0$ and $\eta_e > 0$, we substitute into equations (3.9–3.10) to obtain

$$A\eta_e = \delta A^{(n+1)/n} \left(1 - \frac{\kappa}{A} \right)^{(n+1)/n} \left[1 + \left(\frac{n}{n+1} \right) \frac{\kappa}{A} \right], \quad \eta_e = \sqrt{\frac{2}{A}}. \tag{3.11}$$

Eliminating η_e gives one nonlinear equation to solve for A.

Solutions for several values of the parameter n are shown in Figure 2 with all other parameters kept constant. The self–similar solution retains similarity by constraining the yield surface to be at a constant location along its length as the current spreads. Furthermore the thickness of the plugged region simply grows as the fluid becomes more shear–thinning.

3.1. *Asymptotic analysis for $\alpha \neq 2$*

For $\alpha \neq 2$ no self–similar solution is predicted, but it is possible to find an approximate result starting from the self–similar solution for power–law fluids ($\kappa \to 0$). We briefly recall that for $\kappa \to 0$ equation (3.3) becomes

$$\frac{\partial h}{\partial x} = -\frac{\partial}{\partial x} \left(h \left| \frac{\partial h}{\partial x} \right|^{1/n} \right), \tag{3.12}$$

while the integral mass balance given by equation (3.4) is unmodified. Equations (3.12–3.4) admit the similarity solution

$$h = \eta_N^{n+2} t^{F_2} f(\zeta), \ \eta = x t^{-F_1}, \ \eta_N = \left(\int_0^1 f d\zeta \right)^{-1/(n+2)}, \ \zeta = \eta/\eta_N, \tag{3.13}$$

where

$$F_1 = \frac{\alpha + n}{2 + n}, \quad F_2 = \alpha - F_1, \tag{3.14}$$

and where the shape function f satisfies the following non linear ordinary differential equation

$$\left(f \, |f'|^{1/n} \right)' + F_2 f - F_1 \zeta f' = 0. \tag{3.15}$$

The numerical integration of equation (3.15) for $\alpha \neq 0$ and $\alpha \neq 2$ requires two boundary conditions at $\zeta \to 1$. By assuming $f \approx a_0 (1 - \zeta)^b$, substituting in equation (3.15) and balancing the lower order terms, yields $b = 1$ and $a_0 = F_2^n$. Hence, it follows that

$$f|_{\zeta \to 1 - \epsilon} = F_2^n \epsilon, \quad f'|_{\zeta \to 1 - \epsilon} = -F_2^n, \tag{3.16}$$

with ϵ a small quantity. The two cases $\alpha = 0, 2$ admit an analytical solution with f represented by a parabola and a straight line, respectively.

It is possible to extend the self-similar solution to $\kappa > 0$ with the following expansion in the term $\kappa / |\partial h / \partial x|$ (see, e.g., Sachdev 2000; Hogg *et al.* 2000).

Upon assuming that $\kappa / |\partial h / \partial x|$ is a small quantity, equation (3.3) becomes

$$\frac{\partial h}{\partial t} =$$

$$- \frac{\partial}{\partial x} \left[h \left| \frac{\partial h}{\partial x} \right|^{1/n} \left(1 - \frac{2n + 1}{n(n + 1)} \kappa \left| \frac{\partial h}{\partial x} \right|^{-1} + \frac{n + 1 - 2n^2}{2n^2} \kappa^2 \left| \frac{\partial h}{\partial x} \right|^{-2} + O(\kappa^3) \right) \right]. \tag{3.17}$$

We propose the following expansion in the regime $\sigma \equiv \kappa t^{n(2 - \alpha)/(n+2)} \ll 1$:

$$h = \eta_N^{n+1} t^{F_2} \left[f_0(\zeta) + \sigma f_1(\zeta) + \sigma^2 f_2(\zeta) + \dots \right], \tag{3.18}$$

$$x = \eta t^{F_1} \left(1 + \sigma X_1 + \sigma^2 X_2 + \dots \right), \tag{3.19}$$

where $f_0(\zeta)$ and η_N are given by the similarity solution for power-law fluids (3.13), and $X_1, X_2, \dots$ are constants to be evaluated.

The variable σ is selected in order to guarantee that at the zero order $O(\sigma^0)$ the yield stress contribution is null and the solution is represented by (3.13). At the first order $O(\sigma)$ there is a balance between the terms due to the yield stress and all other terms. The condition $\sigma \ll 1$ requires that $t \ll t_c \equiv \kappa^{(n+2)/[n(\alpha-2)]}$, if $\alpha < 2$, and $t \gg t_c$, if $\alpha > 2$; t_c is defined as a "critical time". Figure 3 shows the critical time $t_c(\kappa, n, \alpha)$ for $\kappa = 0.01$ and for different n and α. The critical time becomes infinite for $\alpha = 2$, notably this coincides with the case which permits a self-similar solution without the necessity of an expansion. It is seen that $\partial t_c / \partial \alpha > 0$ for any n. In addition, $\partial t_c / \partial n > 0$, if $\alpha > 2$, and $\partial t_c / \partial n < 0$, if $\alpha < 2$, hence the domain of validity of the expansion is extended as the fluid becomes more shear–thinning.

The previous analysis implies that for a gravity current of a power–law fluid all terms in the evolution equations evolve at a common rate (or, equivalently, a unique velocity scale exists). In contrast, for a HB fluid the term arising due to the yield stress evolves at a different rate than other terms (i.e. it introduces a second velocity scale, for a given common length scale). In order to obtain an expansion to solve this equation, note that the correction is achieved at first order by computing a second function which evolves with a rate equal to the new one imposed by the yield stress term. The non linearity of the problem requires an increasing number of such terms in the series to improve the accuracy in the balance when extended to higher orders.

However, since κ appears always in powers of $\kappa |\partial h / \partial x|^{-1}$, we expect a reduction in
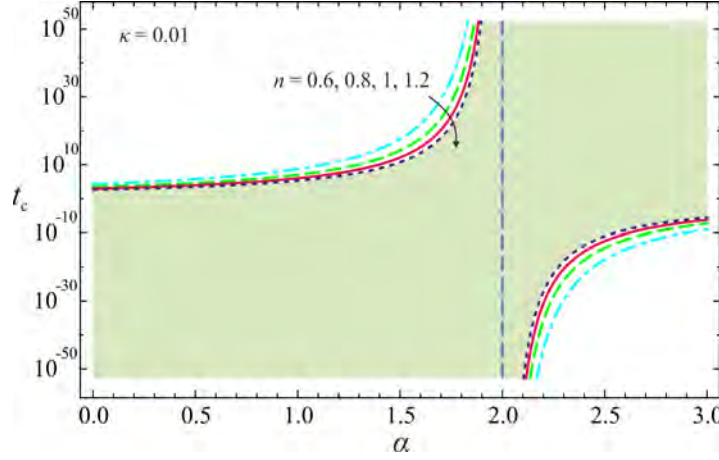
8   *Di Federico et al.*

FIGURE 3. Dimensionless critical time for $\kappa = 0.01$ as a function of the fluid behaviour index n and of α. The vertical dashed line at $\alpha = 2$ is the asymptote, the hatched area indicates the domain where the condition $\sigma < 1$ is satisfied for a fluid with $n = 1.2$.

the accuracy of the asymptotic solution for increasing time, if $\overline{|\partial h/\partial x|} \sim t^{(\alpha-2)n/(n+2)}$ decreases in time, which happens for $\alpha < 2$. Conversely, for $\alpha > 2$, the asymptotic expansion becomes more accurate, but the current evolves to an increasing steepness which renders the thin current assumption asymptotically invalid. The expansion will be uniform in x as long as $|\partial h/\partial x|$ does not approach zero anywhere. In particular, the expansion will be not-uniform if $\alpha = 0$ since in this case the current becomes flat at $x = 0$.

By inserting equations (3.18–3.19) in equation (3.17) and balancing the terms of equal power in σ, at $O(\sigma^0)$ we recover the fundamental balance, with $f_0 \equiv f$ and f represented by (3.13).

At $O(\sigma)$ equation (3.17) becomes

$$\left(f_1 \left| f_0' \right|^{1/n} - \frac{1}{n} f_0 \left| f_0' \right|^{1/n-1} f_1' \right)' + F_2 f_1 - F_1 \zeta f_1' = \frac{1}{\eta_N^n} \frac{2n+1}{n(n+1)} \left(f_0 \left| f_0' \right|^{1/n-1} \right)', \quad (3.20)$$

which is an inhomogeneous linear ODE for the unknown function f_1, with a forcing term modulated by the fundamental solution f_0. The numerical integration of equation (3.20) requires two boundary conditions for $\zeta \to 1$, obtained again by expanding in series near the front of the current. By assuming that $f_1 \approx a_1(1 - \zeta)^b$ (with $f_0 \approx F_2^n(1 - \zeta)$, see equation (3.16)), substituting in equation (3.20) and equating the lower order terms (corresponding to $b = 1$), yields

$$a_1 = \frac{F_2}{(F_2 - F_1 n + F_2 n)} \frac{2n+1}{\eta_N^n (n+1)}, \quad b = 1. \quad (3.21)$$

Hence, the function can be approximated by $f_1 \approx a_1(1-\zeta)$ for $\zeta \to 1$, and the boundary conditions for equation (3.20) are

$$f_1|_{\zeta \to 1-\epsilon} = a_1\epsilon, \ f_1'|_{\zeta \to 1-\epsilon} = -a_1, \quad (3.22)$$

where ϵ is a small quantity.

Even though the two functions f_0 and f_1 are defined in the domain $0 \leqslant \zeta \leqslant 1$, the nose of the current is $\zeta_N = 1 + \sigma X_1 + \ldots$, which is expected to be smaller than unity since the additional resistance supplied by the yield stress reduces the propagation rate

compared to the case $\kappa = 0$. The integral constraint given by equation (3.4) becomes

$$\eta_N^{n+2}(1 + \sigma X_1 + \ldots) \int_0^{1+\sigma X_1 + \ldots} [f_0(\zeta) + \sigma f_1(\zeta)]\, d\zeta = 1, \qquad (3.23)$$

which at $O(\sigma)$ yields

$$X_1 = -\frac{\int_0^1 f_1(\zeta)\, d\zeta}{\int_0^1 f_0(\zeta)\, d\zeta}. \qquad (3.24)$$

Figure 4 shows the correction to the front position for waning inflow rate ($\alpha = 0.5$), constant inflow rate ($\alpha = 1$), waxing inflow rate ($\alpha = 1.5$) and very waxing inflow rate ($\alpha = 2.5$). The case $\alpha = 2$ is not shown since the correction is null. The smallest correction is for waxing inflow rates, with minimum effects for shear-thickening fluids, while for low values of α, the corrections are minor for shear-thinning fluids. The first order correction term may be valid for a limited time, as shown in Figure 4a for shear-thickening and Newtonian fluids with $\kappa = 0.05$; a divergence with the first order approximation solution appears for $t < 10$ and $t < 20$, respectively. Since the critical time is $t_c \approx 100$ and $t_c \approx 400$ for the two cases, we conclude that the limiting factor is the number of terms in the expansion. An extension of the range of validity can be achieved by increasing the number of these terms (see, e.g., Hogg *et al.* 2000).

Figure 5 shows the profiles of the current at $t = 5$ for constant volume ($\alpha = 0$), and constant inflow rate ($\alpha = 1$). The case $\alpha = 0$, $\kappa = 0$ has a closed-form solution (Ciriello *et al.* 2016) and is a parabola for a Newtonian fluid ($n = 1$). The presence of yield stress reduces the front position and increases the average steepness of the profile, without other significant variations as long as κ is a small quantity.

4. 2D flow in a porous medium

The case of flow through a porous medium requires the formulation of the equivalent Darcy's law for a HB fluid, which may be written (Chevalier *et al.* 2013)

$$d\nabla p = \chi \tau_p + \beta \mu_0 \left(\frac{\bar{u}}{d}\right)^n, \qquad (4.1)$$

where d is the diameter of grains, ∇p the pressure gradient, τ_p the yield stress, μ_0 the consistency index, n the flow behaviour index, $\bar{u}$ the darcian velocity, and χ and β are coefficients. The coefficient χ is governed by the maximum width of the widest path of the flowing current, the coefficient β depends on pore size distribution and structure. Their values should, in general, be determined experimentally, and theoretically they are related to the distribution of the second invariant of the strain tensor (Chevalier *et al.* 2014). Here, a pragmatic approach is adopted, and the values reported in Chevalier *et al.* (2013), $\chi = 5.5$ and $\beta = 85$ are used; the diameter of the glass beads employed in our experiments falls in the range adopted in their experiments (from 0.26 to 2 mm). Equation (4.1) indicates that the flow is possible only if $|\partial p/\partial x| > \chi \tau_p/d$, otherwise a plug is formed. Indeed the experiments indicate that percolation takes place even at a very low pressure gradient, with a progressive increment of the flow rate for increasing pressure drop. Chevalier *et al.* (2014) have shown that even at very low darcian velocity values, the region of fluid at rest is negligible and the velocity density distribution is similar to that obtained for a Newtonian fluid.

Under the relevant shallow water approximation, the pressure gradient becomes $\partial p/\partial x = \Delta \rho\, g\, (\partial h/\partial x)$; inverting equation (4.1), and under the constraint $|\partial h/\partial x| > \kappa_p$, the av-
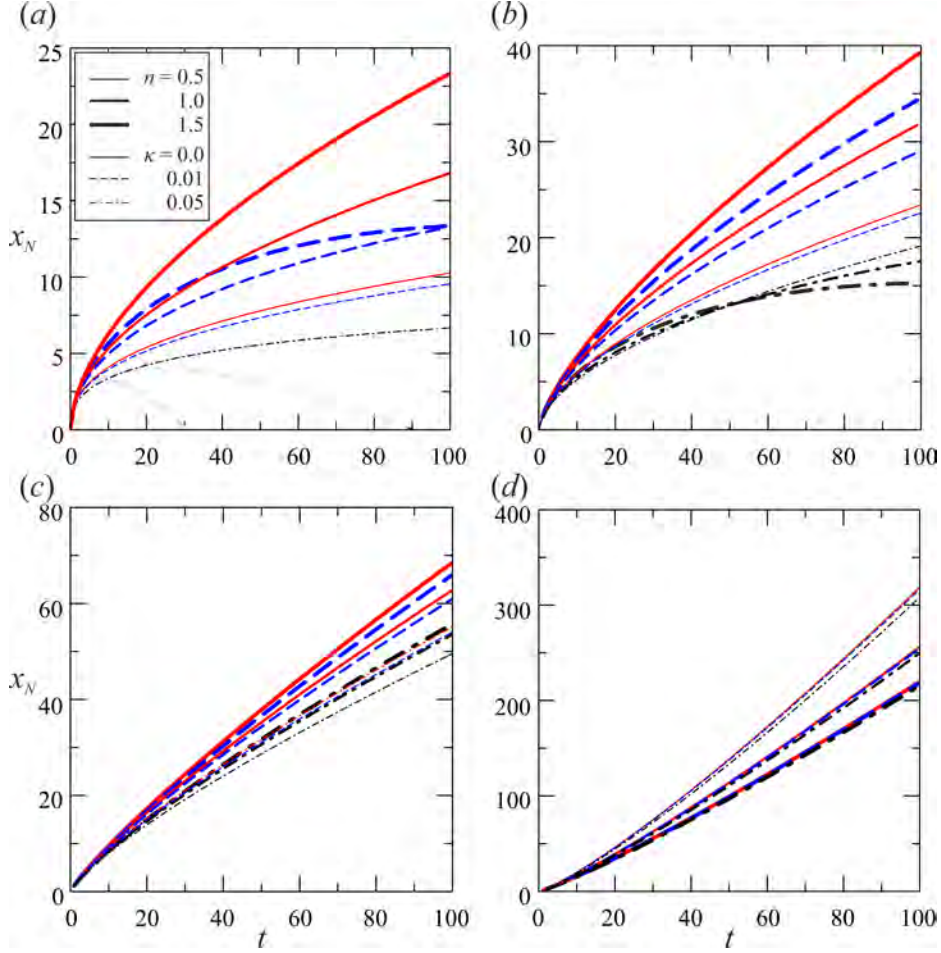
FIGURE 4. The effects of the first order correction on the front position, Hele–Shaw cell. (*a*) $\alpha = 0.5$, (*b*) $\alpha = 1$, (*c*) $\alpha = 1.5$, (*d*) $\alpha = 2.5$. Thick, mid and thin curves refer to $n = 1.5$, $n = 1$, and $n = 0.5$, respectively. Continuous, dashed and dot–dashed curves refer to $\kappa = 0$ (power–law fluid), $\kappa = 0.01$, and $\kappa = 0.05$, respectively. The time decreasing curves, in gray, are unphysical. Variables are non dimensional.

erage velocity is equal to

$$\bar{u} = -\text{sgn}\left(\frac{\partial h}{\partial x}\right) d^{(n+1)/n} \left(\frac{\Delta \rho \, g}{85 \mu_0}\right)^{1/n} \left(1 - \kappa_p \left|\frac{\partial h}{\partial x}\right|^{-1}\right)^{1/n} \left|\frac{\partial h}{\partial x}\right|^{1/n}, \qquad (4.2)$$

where $\kappa_p = 5.5 \tau_p / (d \Delta \rho \, g)$. Inserting the average velocity in the local mass conservation yields for $\partial h / \partial x < 0$

$$\frac{\partial h}{\partial t} = -\frac{d^{(n+1)/n}}{\phi} \left(\frac{\Delta \rho \, g}{85 \mu_0}\right)^{1/n} \frac{\partial}{\partial x} \left[h \left|\frac{\partial h}{\partial x}\right|^{1/n} \left(1 - \kappa_p \left|\frac{\partial h}{\partial x}\right|^{-1}\right)^{1/n}\right], \qquad (4.3)$$

where ϕ is the porosity. Assuming again a current with time variable volume, the integral mass conservation reads

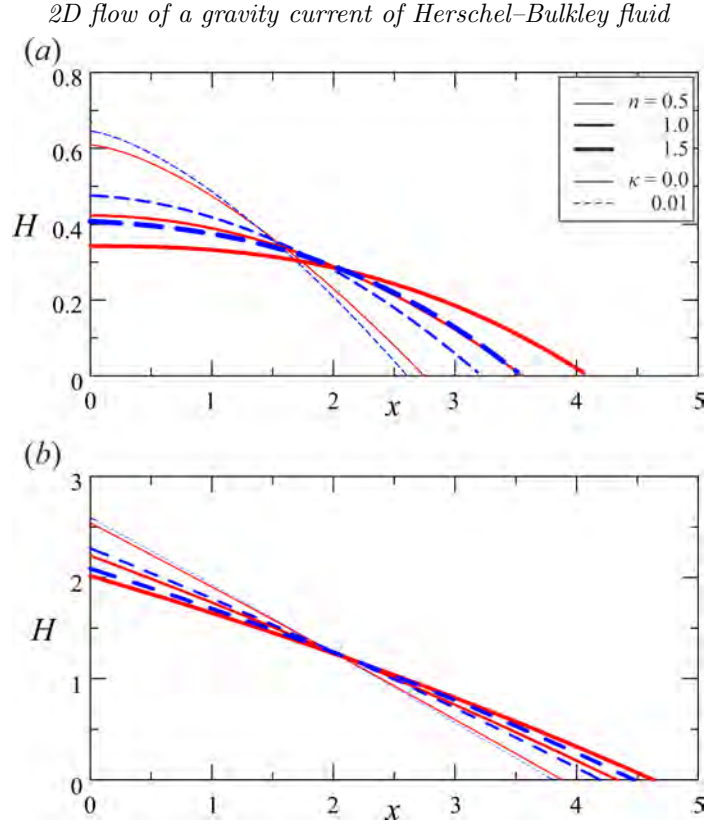$$L_y \phi \int_0^\infty h(x,t) \mathrm{d}x = Q t^\alpha. \qquad (4.4)$$

FIGURE 5. The effects of the first order correction on the current profiles at time $t = 5$, Hele–Shaw cell. (a) $\alpha = 0$, (b) $\alpha = 1$. Thick, mid and thin curves refer to $n = 1.5$, $n = 1$, and $n = 0.5$, respectively. Continuous and dashed curves refer to $\kappa = 0$ (power–law fluid) and $\kappa = 0.01$, respectively. Variables are non dimensional.

Upon introducing the velocity and length scales

$$u^* = \frac{d^{(n+1)/n}}{\phi}\left(\frac{\Delta\rho\,g}{85\mu_0}\right)^{1/n},$$ (4.5)

$$x^* = \frac{d^{(n+1)/n}}{\phi}\left(\frac{Q\phi}{L_y d^{(2n+2)/n}}\right)^{1/(2-\alpha)}\left(\frac{85\mu_0}{\Delta\rho\,g}\right)^{\alpha/[n(2-\alpha)]},$$ (4.6)

with the resulting time scale

$$t^* = \frac{x^*}{u^*} = \left(\frac{Q\phi}{L_y d^{(2n+2)/n}}\right)^{1/(2-\alpha)}\left(\frac{85\mu_0}{\Delta\rho\,g}\right)^{2/[n(2-\alpha)]},$$ (4.7)

equations (4.3–4.4) may be written in non dimensional form as

$$\frac{\partial h}{\partial t} = -\frac{\partial}{\partial x}\left[h\left|\frac{\partial h}{\partial x}\right|^{1/n}\left(1 - \kappa_p\left|\frac{\partial h}{\partial x}\right|^{-1}\right)^{1/n}\right],$$ (4.8)

$$\int_0^\infty h(x,t)\mathrm{d}x = t^\alpha.$$ (4.9)

As for the flow in the fracture, equations (4.8-4.9) admit a self similar solution only for

$\alpha = 2$, which breaks down the scales in equations(4.6–4.7). By defining an arbitrary time scale t^*, the new velocity scale $u^* = (Q/L_y\phi)^{1/2}$ and the coefficient

$$\delta_p = \left(\frac{L_y d^{(2n+2)/n}}{Q\phi}\right)^{1/2} \left(\frac{\Delta\rho\, g}{85\mu_0}\right)^{1/n}, \tag{4.10}$$

which is the ratio between the velocity scale (4.5) and the new velocity scale, equation (4.3) may be written in non dimensional form (the tilde is dropped) as

$$\frac{\partial h}{\partial t} = -\delta_p \frac{\partial}{\partial x}\left[h\left|\frac{\partial h}{\partial x}\right|^{1/n}\left(1 - \kappa_p\left|\frac{\partial h}{\partial x}\right|^{-1}\right)^{1/n}\right], \tag{4.11}$$

while equation (4.4) becomes

$$\int_0^\infty h(x,t)\mathrm{d}x = t^2. \tag{4.12}$$

The self similar solution is again $h = tf(\eta)$, $\eta = x/t$, and substituting into equation (4.11) gives

$$f - \eta f' = -\delta_p \left[f\,|f'|^{1/n}\left(1 - \frac{\kappa_p}{|f'|}\right)^{1/n}\right]'. \tag{4.13}$$

The system of equations (4.11–4.12) admits a solution $f(\eta) = A_p(\eta_{ep} - \eta)$, which upon substitution yields

$$\frac{2}{A_p} = \delta_p^2(A_p - \kappa_p)^{2/n}, \quad A_p\eta_{ep}^2 = 2. \tag{4.14}$$

For given values of κ_p and δ_p, it is possible to solve the first equation numerically in the unknown A_p and then to compute η_{ep}. The condition for flow requires that $A_P > \kappa_p$. The general case $\alpha \neq 2$ can be treated with an expansion similar to that adopted for the flow in a Hele–Shaw cell.

There are many conceptual and formal similarities between the equations arising in the description of Hele–Shaw and 2D porous flows of a HB fluid, while the main point of difference is the treatment of plug. While in a Hele–Shaw flow the presence of a plug region is an explicit part of the model (possibly with wall slip), for a porous flow the model predicts the cessation of the flow below a threshold within the entire body of the granular medium. During the experiments described in the following, it was noted that below a threshold value of the pressure gradient ($\partial h/\partial x$ in our approximation), a percolation develops and the flow never completely stops. This behaviour suggests that a bi-viscous model, able to smooth the transition from pre- to post-yield behaviour, could better interpret the experiments.

5. The experiments

In order to validate the theoretical model, two series of experiments were conducted (i) in a Hele–Shaw cell with a small gap, simulating a fracture, and (ii) in the same cell with a larger gap and filled with glass beads of uniform size, reproducing a 2D porous medium. Figure 6 shows the experimental device and two different snapshots. The 75 cm long cell was made of two parallel plates of transparent plastic, the gap width between which could be varied as necessary. In order to limit slip for the experiments without glass beads, a commercial transparent anti–slip tape was used to line the inside of the plates. Fluid was injected with a syringe pump for the fracture tests, and with a vane pump controlled by an inverter for the porous flow tests requiring higher flow rates.

The HB fluids were obtained by mixing deionized water, Carbopol 980 (0.05% to 0.14%), ink, with subsequent neutralization by adding NaOH. The mass density was measured with a hydrometer (STV3500/23 Salmoiraghi) or with a pycnometer, with an accuracy of 1%.

The rheologic behaviour of the fluid was analysed in a parallel plate rheometer (Dynamic Shear Rheometer Anton Paar Physica MCR 101) conducting several different tests, both static and dynamic, to evaluate the fluid behaviour index, the consistency index and the yield stress. When dealing with non-Newtonian fluids, either Ostwald–de Waele (power–law) or Herschel-Bulkley, the characterisation of the correct parameters representing the rheological behaviour of the fluid can be challenging. However the final aim of the experiments is clear, and that is to verify the proposed model by using independent measurements of both the flow field characteristics (front position and current thickness over time) and of the fluid rheometric parameters. Noteworthy, the models used to describe the fluid rheology and obtain the rheometric parameters do not have a general validity but are an approximation of the fluid behaviour in a limited shear range. Furthermore, none of the flow fields generated in the measuring instruments (mainly rheometers) is perfectly viscometric. The problem of correctly estimating the rheometric parameters is particularly significant for HB fluids, for which yield stress estimation (and definition) is far from trivial. See the review paper by Nguyen & Boger (1992) for a discussion on the topic and a description of the methodology adopted in our laboratory experiments. Therefore in order to evaluate the accuracy of the measurements of the yield stress, we carried out numerous additional experiments with different methods, broadly classified as "direct" and "indirect" methods, see the further description in Appendix A.

The glass beads forming the porous medium had a nominal diameter of 3, 4 and 5 mm ± 0.1 mm depending on the test. The profile of the current was detected with either a stills camera (Canon EOS 3D, 3456×2304 pixels) operating at a rate of 0.5 frames s^{-1} or a high-resolution video camera (Canon Legria 1920×1080 pixels) operating at 25 frames s^{-1}. The images were then post-processed with a proprietary software package in order to be referenced to a lab coordinate system and for the boundary between the (dark) intruding current and the empty cell or the (light) porous medium to be extracted and parameterised. With this set-up, the overall accuracy in detecting the profile of the current was approximately 1 mm, whilst the uncertainty in measuring timings was negligible. During all experiments, the natural packing prevented any movement of the beads, as demonstrated by the images used for extracting the fluid interface.

Table 1 and Table 2 list the parameters for the two sets of experiments (fracture and 2D porous medium) and four series with increasing concentration of Carbopol (labelled from A to D, corresponding to 0.05%, 0.08%, 0.10%, and 0.14% concentration respectively). Figure 7a shows the dimensionless front position of the currents versus time for thirteen tests conducted in the fracture with three different HB fluids. The plotting variables have been chosen to collapse all the experimental data into a single line. In order to separate the results for the three different fluids, the experimental front position was multiplied by 0.5 and 1.5 for experiments A and C, respectively. The uncertainty in the model and experimental data was computed following the same procedure reported in Di Federico *et al.* (2014), and is represented by the dashed lines and error bars corresponding to plus or minus one standard deviation (STD) for the data. The front propagation is generally linear for all tests, with some discrepancy at early times due to the effects of the injection geometry and the poor adherence of the experiments to model assumptions. We recall that the solution is an "intermediate asymptotic" to the general solution, and is valid for times and distances from the boundaries large enough to forget the details of the boundary (or initial) conditions but far enough from the ultimate asymptotic state of
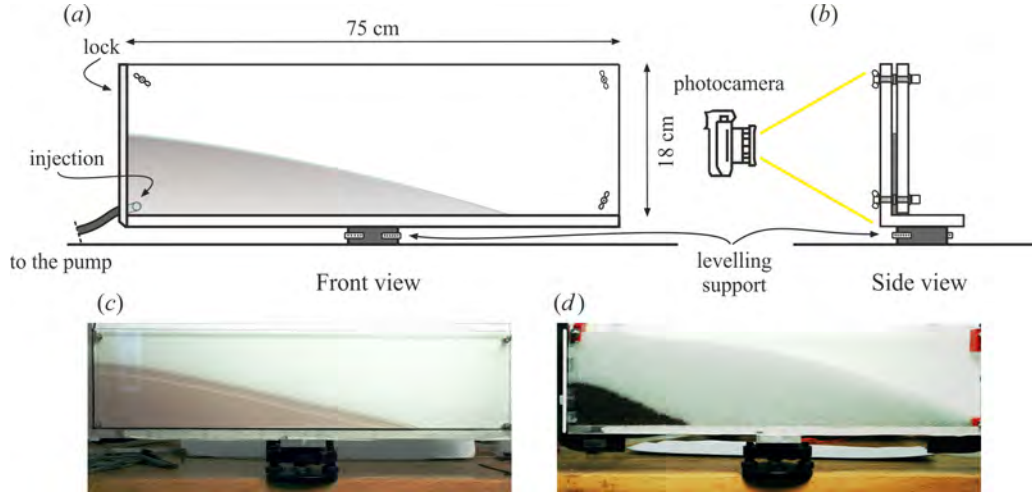
FIGURE 6. A sketch of the experimental rectangular channel. (a) Front view, (b) side view, (c) a snapshot of the channel during Exp. B1 (the shaded area is the advancing current), and (d) a snapshot of the channel filled with glass beads during Exp. A1 (the dark area is the advancing current,the grey area is the porous medium not yet reached by the current).

Exp.	Q (cm^3 s^{-2})	L_y (cm)	n	μ_0 (Pa s^n)	τ_p (Pa)	ρ (kg m^{-3})	κ ($\times 10^{-3}$)	$\dot{x}_{N-exp}$ (cm s^{-1})	$\dot{x}_{N-theor}$ (cm s^{-1})	fluid
B1	0.012	0.32	0.68	0.9	0.3	1000	19	0.55	0.54	Carb. 0.08%
B2	0.012	0.48	0.68	0.9	0.3	1000	13	0.53	0.54	
B3	0.024	0.48	0.68	0.9	0.3	1000	13	0.71	0.71	
B4	0.024	0.48	0.68	0.9	0.3	1000	13	0.73	0.71	
C1	0.006	0.48	0.66	2.5	0.6	1000	30	0.29	0.28	Carb. 0.10%
C2	0.012	0.48	0.66	2.5	0.6	1000	30	0.37	0.37	
C3	0.012	0.48	0.66	2.5	0.6	1000	30	0.38	0.36	
C4	0.024	0.48	0.66	2.5	0.6	1000	30	0.46	0.48	
C5	0.024	0.48	0.66	2.5	0.6	1000	30	0.53	0.48	
D1	0.006	0.48	0.45	3.1	15.0	1000	637	0.16	0.18	Carb. 0.14%
D2	0.012	0.48	0.45	3.1	15.0	1000	637	0.22	0.22	
D3	0.012	0.48	0.45	3.1	15.0	1000	637	0.23	0.23	
D4	0.024	0.48	0.45	3.1	15.0	1000	637	0.31	0.30	

TABLE 1. Parameters for the experiments in the fracture. The injected volume scales with t^2.

the system. Hence, we expect that also for longer time the experimental results will deviate from the self–similar solution.

Figure 7b shows the shape of the current at different times for Exp. B3. The normalized profiles show a fairly good collapse to a single curve, even though the discrepancy between experiments and theory becomes evident for $\eta/\eta_e < 0.30$ and near the front. This is due to the disturbances at the inlet (the inflow is located near the bottom in the experiments, while assumed to be evenly distributed along the vertical in the theory), to non–negligible vertical velocities near the inlet (see Longo & Di Federico 2014), and to the bottom stress, which becomes relevant at the tip of the current. The experimental profiles are similar for all other tests.
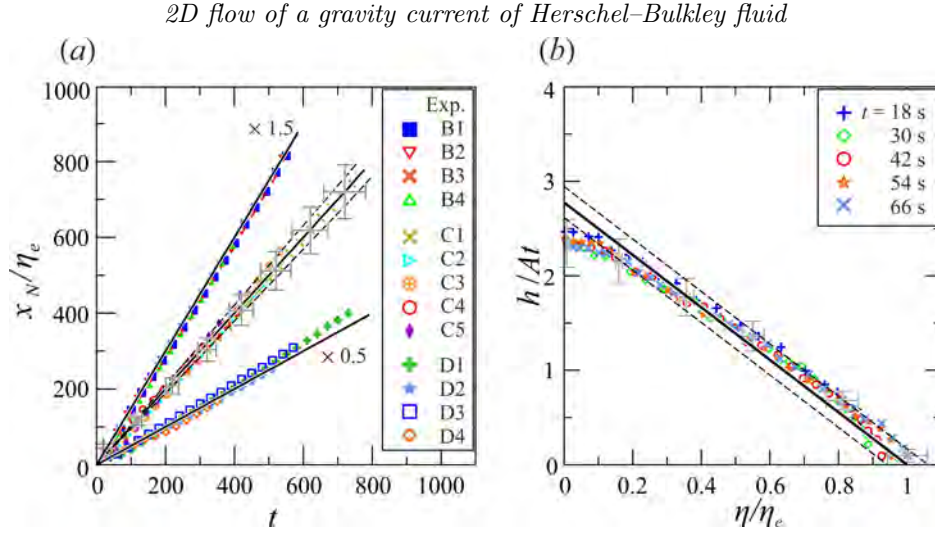
FIGURE 7. A comparison of theory with experiments for the fracture, showing (a) the front position x_N/η_e as a function of dimensionless time t for all tests. The three bold lines represent the perfect agreement with theory for the three different fluids used in the experiments; (b) the dimensionless profile of the current at different times for Exp. B3. The error bars refer to the profile at $t = 66$ s and correspond to $\pm$ one STD, the bold straight line indicates the theoretical profiles and the dashed lines are the confidence limits of the model. For clarity, in (a,b) one point of every three is plotted.

Exp.	Q (cm^3 s^{-2})	α	d (cm)	L_y (cm)	n	μ_0 (Pa s^n)	τ_p (Pa)	ρ (kg m^{-3})	κ_p ($\times 10^{-3}$)	$\dot{x}_{N-exp}$ (cm s^{-1})	$\dot{x}_{N-theor}$ (cm s^{-1})	fluid
A1	0.100	2	0.3	3	0.70	0.2	0.1	1000	19	0.76	0.72	Carb. 0.05%
A2	0.200	2	0.4	4	0.70	0.2	0.1	1000	14	1.06	1.00	
B5	0.025	2	0.5	5	0.68	0.9	0.3	1000	34	0.23	0.23	Carb. 0.08%
C6	0.020	2	0.4	4	0.60	2.5	0.6	1000	84	0.17	0.16	Carb. 0.10%
C7	0.030	2	0.5	5	0.60	2.5	0.6	1000	67	0.17	0.17	
C8	0.030	2	0.4	3	0.60	2.5	0.6	1000	84	0.17	0.17	
A3	16.0	1.0	0.3	3	0.70	0.2	0.1	1000	18			Carb. 0.05%
A4	26.0	0.6	0.4	4	0.70	0.2	0.1	1000	14			
B6	4.0	1.0	0.5	5	0.68	0.9	0.3	1000	30			Carb. 0.08%
B7	30.0	0.6	0.5	5	0.68	0.9	0.3	1000	30			

TABLE 2. Parameters of the experiments in a porous medium, with volume $\propto t^\alpha$. The experimental and theoretical front speed is not constant for the last four experiments.

Figure 8a shows the front position for the six experiments conducted in a porous medium with three different HB fluids. The profile was corrected for capillary effects following the procedure outlined in Longo *et al.* (2013b). The front velocity shows a fairly good agreement with the theoretical constant velocity, even though asymptotically there are larger discrepancies due to the geometry of the current, with a very thin nose affected by the bottom boundary effects. The experimental profiles of the current at different times are shown in Figure 8b for Exp. A2. The profiles collapse to a single curve, which is significantly affected by the disturbances at the inlet. The experimental points are within the confidence limits of the theoretical models and show a clear linearity for $\eta > 0.5\eta_{ep}$. In order to also check the model for the asymptotic solution with $\alpha \neq 2$, some experiments were designed for constant ($\alpha = 1$) and waning ($\alpha = 0.6$) inflow
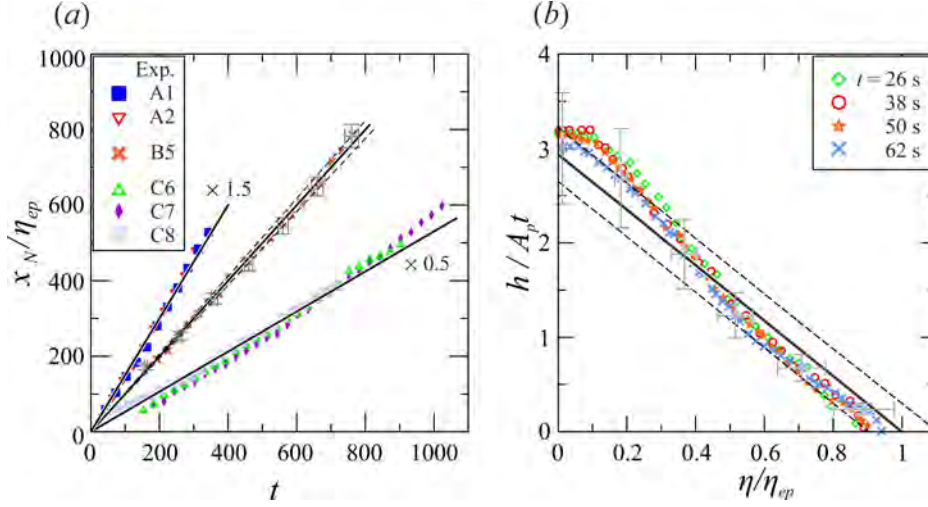
FIGURE 8. A comparison of theory with experiments for 2D porous flow (rectangular channel filled with glass beads). For caption see Figure 7. (b) refers to Exp. A2.
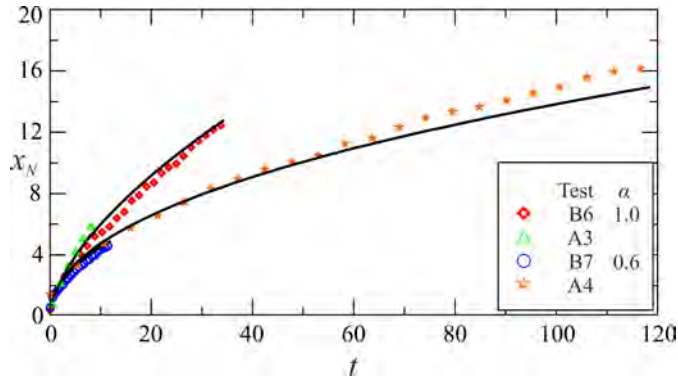

FIGURE 9. A comparison of theory (solid curves) with experiments (symbols) for the 2D porous medium, showing x_N as a function of dimensionless time t for all tests. The injected volume scales with t^α. Experimental parameters are listed in Table 2.

rate, with two different HB fluids and three different bead diameters (see the last four experiments in Table 2). Figure 9 shows the experimental front position (symbols) and the first order expansion of the self-similar solution (solid curves). The overlap in each case is satisfactory, in particular for experiments at constant inflow rate.

6. Conclusions

A general model was developed for gravity-driven flows of Herschel–Bulkley (HB) fluids in a narrow fracture or 2D porous media, extending existing formulations for Newtonian and power-law fluids. For the special case of an inflow rate linearly time-increasing, a self–similar solution was derived for both cases: the front of the current advances at constant speed and with a linear profile. For the general case of power–law inflow rate, an expansion of the self–similar solution valid for an Ostwald–de Waele fluid was developed, in the limit $\kappa \ll 1$ or $\kappa_p \ll 1$, with these two parameters marking the deviation form pure power-law behaviour. The expansion has a validity controlled by the value of α;

hence, it is valid within a time interval limited by a critical time value, beyond which either the approximation in deriving the differential equation, or the adopted expansion become invalid.

The rheological parameters of the HB fluids have been measured with independent tests, with two different rheometers and with both direct and indirect methods for the yield stress. The results for the yield stress vary according to the different methods adopted, however a single value of the yield stress (the lowest in the list of measured values) has proven to correctly characterise all the experiments performed with the same fluid in the Hele–Shaw cell and in the porous medium.

The experiments were mostly conducted with volume scaling in time as $\alpha = 2$, with some additional experiments conducted with $\alpha = 0.6\,, 1$. Each test shows a reasonable agreement with the theory for flow in fractures and porous media, especially so for the former. Deviations from the linear profile forecast for $\alpha = 2$ occur near the inlet; in the 2D porous medium, a dome develops near the inlet, followed by a profile in good agreement with the theory. In all cases the theoretical prediction lies within the confidence limits of the experimental data. These experimental results provide a verification of the flow model for HB fluids in fractures and also a further verification of the extended Darcy's law proposed by Chevalier *et al.* (2013) for HB fluid flow in porous media. However the existence of non–zero Darcy flow below the threshold pressure gradient requires further fundamental experimental investigation.

An additional promising area of research suggested by our work is the interaction of rheologically complex fluids (described e.g. by the HB model) with spatial heterogeneity in key problem parameters, using either a deterministic or stochastic approach. For fracture flow, heterogeneity may be represented by a spatially variable aperture (Lavrov 2013), or by obstructions, local contractions and expansions (Hewitt *et al.* 2016). For porous media flow, spatial variability of permeability may be modelled using deterministic trends or directly as a random field, using approaches and methods typical of stochastic hydrology. We are currently working on these problems and plan to report on our efforts in the near future.

Appendix A. Rheometry of the fluids

Most measurements were conducted with a parallel plate rheometer (Dynamic Shear Rheometer Anton Paar Physica MCR 101, equipped with a moving plane plate of diameter 25 mm, gap equal to 1mm in most cases), and with a strain-controlled rheometer (coaxial cylinders Haake RT 10 RotoVisco, equipped with cup and rotor according to DIN 53019, with internal radius equal to 19.36 mm and external radius equal to 21 mm). In order to limit the slip, the surfaces of the cup and of the rotor were roughened with strips of Sellotape, the surface of the plates were roughened with sand paper P-60 glued on the smooth surface (see Carotenuto & Minale 2013, for an in depth analysis of the effects of sandpaper on rheological measurements of Newtonian fluids). Additionally, in order to prevent absorption, the sand paper was painted with transparent acrylic.

Figure A.1*a* shows the classical stress strain-rate experimental results obtained with the coaxial cylinders rheometer, Figure A.1*b* shows similar results for the fluid 0.10% obtained with the plane plate rheometer. The continuous curves represent the HB model interpolation for the reduced series of experimental points, visualized with filled symbols. The reduction of the sample is required partly due to the limits of accuracy of the instruments at very low shear-rate, partly as a consequence of the poor adaptation of the model to the real rheological behaviour of the fluid. This is the simplest and most common procedure to estimate the yield stress, but the results depend on the cut-off value
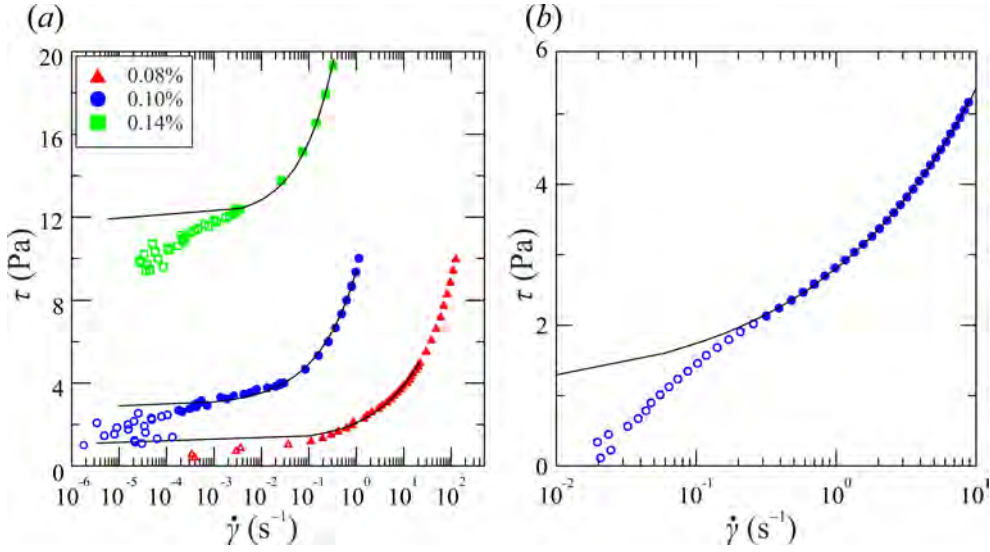
FIGURE A.1. (*a*) Experimental shear–stress shear–rate curves for three fluids Carbopol 980 0.08, 0.10, 0.14%. Measurements with the coaxial cylinders rheometer. (*b*) Experimental shear–stress shear–rate curves for Carbopol 980 0.10%. Measurements with the plane plate rheometer. The curves are the HB model interpolation for the reduced series of experimental points, represented by the filled symbols.

of shear–rate used to select the reduced sample. For the present data, $\tau_p = 1.1$, 2.9, 7 Pa for measurements in the coaxial cylinders rheometer and for fluids with increasing concentration of Carbopol. For measurements taken with the parallel plate rheometer, the yield stress for the mixture with 0.10% of Carbopol 980 is equal to 1.3 Pa. This method of estimation of the yield stress is an indirect one.

A direct method is based on stress relaxation: the fluid is sheared reaching a specific value of strain, then shearing stops and the shear stress requested to guarantee the reached strain is recorded. Its asymptotic value is taken to be equal to the yield stress. Figure A.2*a* shows the results for various strains in the fluid Carbopol 980 0.10%. The asymptotic value lies in he range $0.6 - 1.0$ Pa and is a function of the imposed strain; it decays for increasing strain, since the degree of disturbances in the fluid controls the late behaviour of the system. Figure A.2*b* shows the asymptotic shear stress for imposed shear–rate. After an initial growth, the shear–stress reaches a plateau, up to a limiting value which makes the transient state extremely long. The stress corresponding to the minimum reached plateau is assumed as an upper limit of the yield stress. For the 0.10% Carbopol 980 fluid, $\tau_{min} \approx \tau_p = 1.15$ Pa.

Another method is called *creep and recovery*: a constant shear stress is applied in steps and the creep is observed. If a more or less complete recovery is reached, then the applied stress was below the yield stress and the continuum behaved as an elastic solid. If a limited or null recovery is reached, then the applied stress was above the yield stress. Figure A.3*a* shows strain-times curves for Carbopol 980 0.10%, with stress imposed for 20 s (except for the curve relative to $\tau = 1$ Pa), and a recovery for 30 s. Figure A.3*a* shows the corresponding time evolution of apparent viscosity. The residual strain is equal to 28, 32, 54, 85% for $\tau = 0.2$, 0.5, 1, 1.5 Pa, respectively, and the yield stress is assumed in the range $[1 - 1.5]$ Pa. The estimation is affected by a significant uncertainty, because in the present experiments the residual deformation is monotonic with the imposed stress
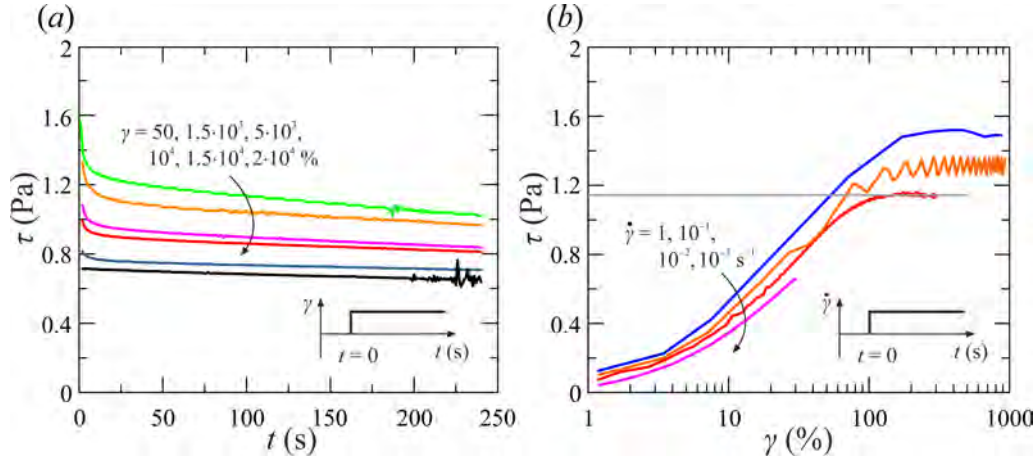
FIGURE A.2. Carbopol 980 0.10%.(*a*) Asymptotic stress at constant strain; (*b*) asymptotic stress at constant strain–rate. The insets show the procedure adopted in testing.
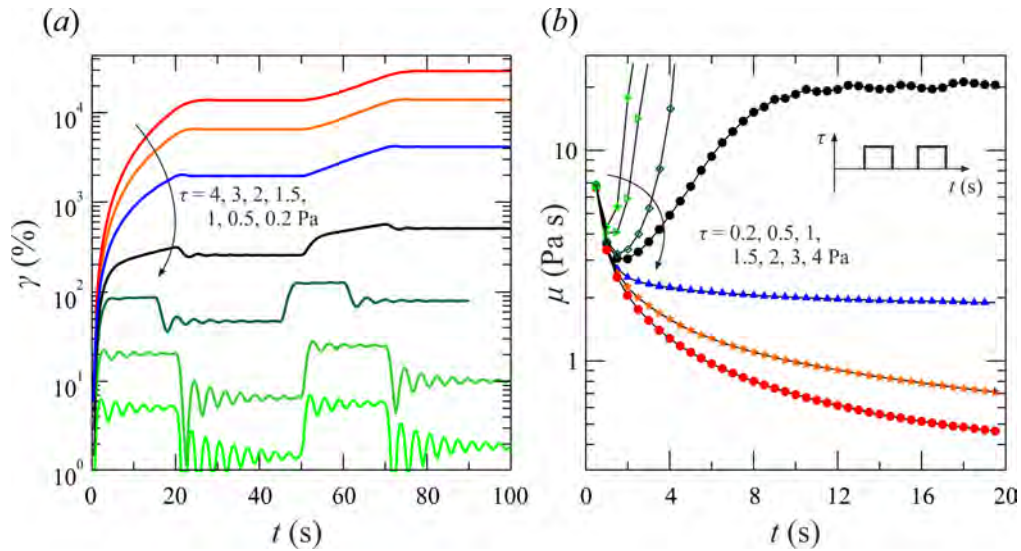

FIGURE A.3. Creep-recovery method for the Carbopol 980 0.10%. (*a*) Strain-times curves, and (*b*) corresponding apparent viscosity. The yield stress lies between $\tau = 1\,\mathrm{Pa}$ and $\tau = 1.5\,\mathrm{Pa}$. Measurements were conducted with the parallel plate rheometer; the inset shows the procedure adopted for testing.

and no abrupt increasing is observed. For other fluids, the behaviour is much sharper (Magnin & Piau 1987).

The yield stress was also measured with a direct method based on the static stability of a layer of fluid on an inclined plane (Uhlherr *et al.* 1984), by adopting the same device and experimental technique detailed in Longo *et al.* (2016). The yield stress can be evaluated by assuming that at the incipient motion the following balance holds:

$$\tau_p = \rho g h \sin \theta_c, \qquad (A\,1)$$

where h is the thickness of the layer and θ_c the critical angle.

The incipient motion of the free surface, as detected with a particle image velocity
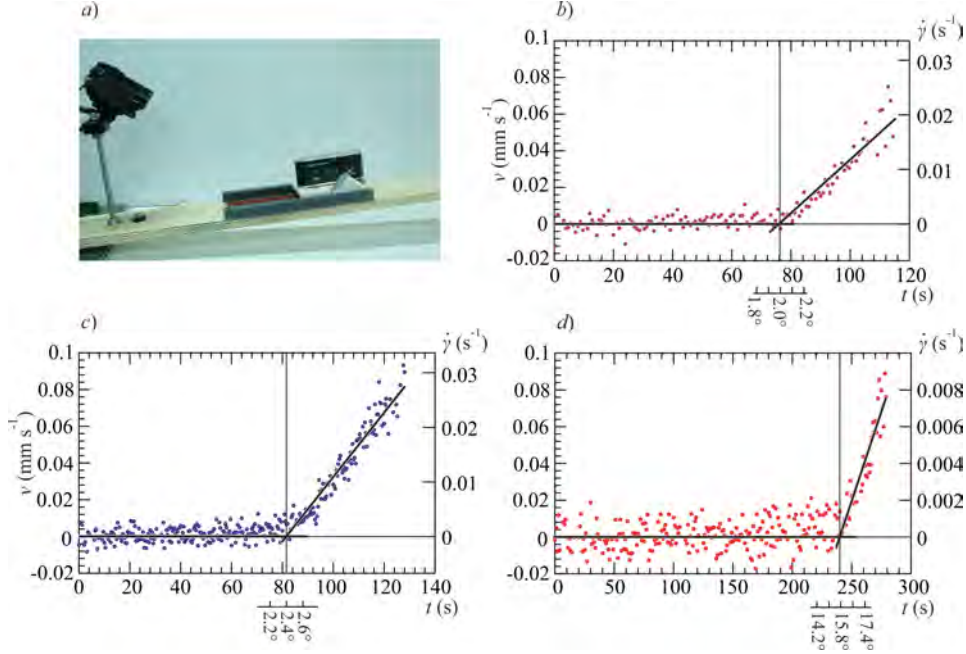
FIGURE A.4. (a) A photo of the inclined plane and of the accessories used for a direct measurement of the yield stress. The electronic level and the video camera are in the same frame of the fluid layer; (b) the plots of the free surface velocity versus time for a mixture of Carbopol 980 (0.08% neutralized); (c) a mixture of Carbopol 980 (0.10% neutralized); (d) a mixture of Carbopol 980 (0.14% neutralized). The solid lines indicate the fitted free surface velocity, the vertical solid line indicates the assumed start of flow motion. The secondary horizontal axis indicates the angle with respect to the horizontal, the secondary vertical axis indicates the average shear rate obtained by dividing the free surface velocity and the starting thickness of the layer, neglecting its reduction in time. The thickness of the layer was set to 0.3, 0.3 and 1 cm, for Carbopol 980 0.08, 0.10, 0.14%, respectively.

algorithm applied to the images recorded by a videocamera, is assumed as indicator of the sliding. Figure A.4 shows, for three different yield stress fluids, the experimental apparatus and the plots of the free surface for increasing bottom inclination. The dots represent the average velocity of the free surface, with dispersion due to vibrations and to noise in the images. It is possible to detect a kink, enhanced by separately interpolating the pre–motion and the post–motion experimental data with two different straight lines. However, a creep motion is detected near the critical angle, presumably due to the elastic deformation of the layer of material before flowing.

The overall uncertainty, computed as

$$\frac{\mathrm{d}\tau_p}{\tau_p} = \frac{\mathrm{d}\rho}{\rho} + \frac{\mathrm{d}h}{h} + \frac{\mathrm{d}\theta_c}{\tan\theta_c}, \tag{A 2}$$

has a significant contribution due to the uncertainty on the thickness of the layer h. By assuming that the critical angle is detected within the uncertainty of the electronic level ($\pm 0.1\,\mathrm{deg}$), and assuming an uncertainty in the thickness measurements equal to $\pm 0.3\,\mathrm{cm}$, the estimated yield stress values are $\tau_p = 1.0 \pm 0.1\,\mathrm{Pa}$, $\tau_p = 1.2 \pm 0.2\,\mathrm{Pa}$, $\tau_p = 26 \pm 1\,\mathrm{Pa}$ for Carbopol 980 0.08, 0.10, 0.14%, respectively. However, the true uncertainty is larger than our estimate, due to the intrinsic uncertainty in the definition of the critical angle.

Another method to estimate the yield stress is based on the dynamic behaviour at small deformation, as detected with oscillatory shear tests, with the measurement of the
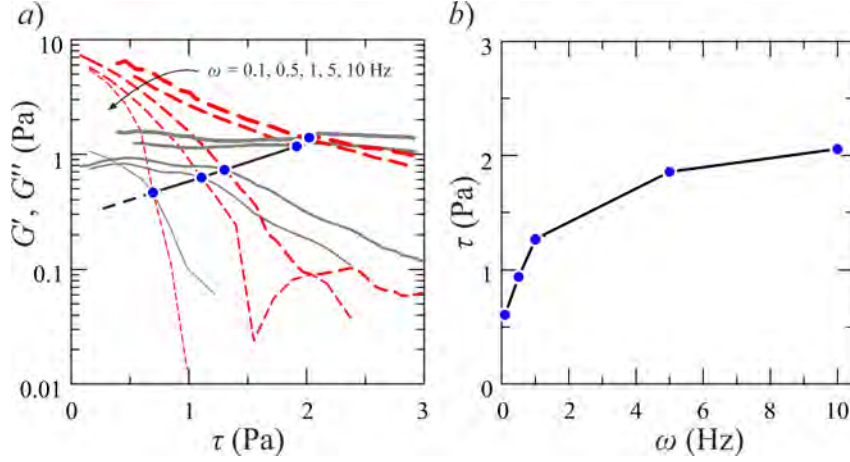
FIGURE A.5. (*a*) Evolution of the storage modulus G' (red dashed lines) and of loss modulus G'' (gray continuous lines) for mixture Carbopol 980 0.10% as a function of stress for different frequencies. The symbols are the intersection between the moduli (cross over), conventionally representing the flow point; (*b*) cross over stress as a function of the frequency. Measurements with parallel plate rheometer, gap 1 mm, $T = 298\,\mathrm{K}$.
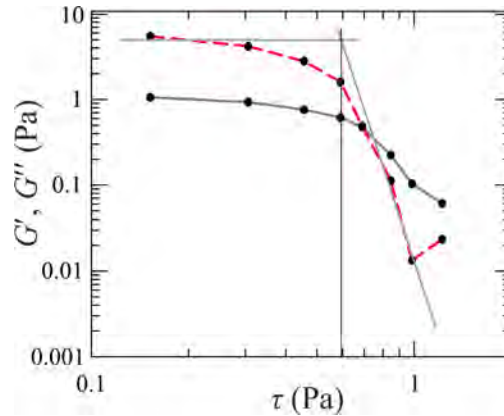

FIGURE A.6. Sweep experiments of Carbopol 980 0.10% at frequency $\omega = 0.1\,\mathrm{Hz}$. The yield stress is evaluated as the abscissa of the intersection of the two straight lines interpolating the storage modulus G' in the left and in the right sides of the cross over, respectively.

storage modulus $G'(\omega)$ and the loss modulus $G''(\omega)$, representative of the elastic and of the viscous behaviour of the continuum, respectively. Applying a sinusoidal strain $\gamma = \gamma_0 \sin \omega t$ with small amplitude γ_0 and frequency ω, the time varying stress is measured $\tau = \tau_0 \sin(\omega + \delta t)$, where δ is a phase shift. The complex modulus $G^*(\omega) \equiv \tau/\gamma = G'(\omega) + iG''(\omega)$ has the two components, G' and G'', representative of elasticity (perfect if $G'' = 0$, $\delta = 0$) and of viscosity (perfect if $G' = 0$, $\delta = 90°$), respectively. The yield stress can be estimated as the intercept of the tangent of the storage modulus considering the domains before after the cross over (De Graef *et al.* 2011). Figure A.5*a* shows the moduli measured at different frequencies for Carbopol 980 0.10%, while Figure A.5*b* shows the cross over variation with the frequency ω. Selecting the lowest frequency measurements ($\omega = 0.1\,\mathrm{s}^{-1}$), the yield stress can be estimated as shown in Figure A.6, obtaining $\tau_y \approx 0.6\,\mathrm{Pa}$.

Table 3 lists the estimated yield stress adopting the different techniques for the fluid

Method	see:	τ_p (Pa)
Extrapolation rheom. 1	Fig. A.1*a*	2.9
Extrapolation rheom. 2	Fig. A.1*b*	1.3
Stress relaxation (constant strain)	Fig. A.2*a*	0.6–1
Asymptotic stress (constant strain–rate)	Fig. A.2*b*	< 1.1
Creep–recovery	Fig. A.3	1–1.5
Inclined plane	Fig. A.4*c*	1.2
Dynamic oscillatory	Fig. A.6	0.6

TABLE 3. Synthesis of the yield stress estimations for Carbopol 980 0.10%. Rheom. 1 refers to the coaxial cylinders rheometer, rheom. 2 refers to the parallel plate rheometer.

Carbopol 980 0.10%. The results indicate the dispersion of the data and that measurements can give at most a range of variation of the yield stress to be used for the verification of the theoretical models.

REFERENCES

ANCEY, C. & COCHARD, S. 2009 The dam-break problem for Herschel-Bulkley viscoplastic fluids down steep flumes. *Journal of Non-Newtonian Fluid Mechanics* **158**, 18–35.

BALMFORTH, N.J., CRASTER, R.V., RUST, A.C. & SASSI, R. 2006 Viscoplastic flow over an inclined surface. *Journal of Non-Newtonian Fluid Mechanics* **139**, 103–127.

BARLETTA, A. & DE B. ALVES, L.S. 2014 On Gill's stability problem for non-Newtonian Darcy's flow. *Int. J. Heat Mass Transfer* **79**, 759–768.

CANTELLI, A. 2009 Uniform flow of modified Bingham fluids in narrow cross sections. *J Hydraul. Eng.* **135**, 640–650.

CAROTENUTO, C. & MINALE, M. 2013 On the use of rough geometries in rheometry. *Journal of Non-Newtonian Fluid Mechanics* **198**, 39–47.

CARREAU, P. J. 1972 Rheological equations from molecular network theories. *Transactions of The Society of Rheology* **16** (1), 99–127.

CHAMBON, G., GHEMMOUR, A. & NAIIM, M. 2014 Experimental investigation of viscoplastic free-surface flows in a steady uniform regime. *J. Fluid Mech.* **754**, 332–364.

CHEVALIER, T., CHEVALIER, C., CLAIN, X., DUPLA, J.C., CANOU, J., RODTS, S. & COUSSOT, P. 2013 Darcy's law for yield stress fluid flowing through a porous medium. *Journal of Non-Newtonian Fluid Mechanics* **195**, 57–66.

CHEVALIER, T., RODTS, S., CHATEAU, X., CHEVALIER, C. & COUSSOT, P. 2014 Breaking of non-Newtonian character in flows through a porous medium. *Phys. Rev. E* **89**, 023002.

CIRIELLO, V., LONGO, S., CHIAPPONI, L. & DI FEDERICO, V. 2016 Porous gravity currents: a survey to determine the joint influence of fluid rheology and variations of medium properties. *Advances in Water Resources* **92**, 105 – 115.

COUSSOT, P. 2014 Yield stress fluid flows: A review of experimental data. *Journal of Non-Newtonian Fluid Mechanics* **211**, 31 – 49.

CRISTOPHER, R. H. & MIDDLEMAN, S. 1965 Power-law flow through a packed tube. *Ind. Eng. Chem. Fundam.* **4**, 422–427.

CROSS, M. M. 1965 Rheology of non-Newtonian fluids: a new flow equation for pseudoplastic systems. *Journal of colloid science* **20** (5), 417–437.

DE GRAEF, V., DEPYPERE, F., MINNAERT, M. & DEWETTINCK, K. 2011 Chocolate yield stress as measured by oscillatory rheology. *Food Research International* **44** (9), 2660–2665.

DI FEDERICO, V., ARCHETTI, R. & LONGO, S. 2012*a* Similarity solutions for spreading of a

two-dimensional non-Newtonian gravity current. *J. Non-Newton. Fluid Mech.* **177–178**, 46–53.

DI FEDERICO, V., ARCHETTI, R. & LONGO, S. 2012*b* Spreading of axisymmetric non-Newtonian power-law gravity currents in porous media. *J. Non-Newton. Fluid Mech.* **189–190**, 31–39.

DI FEDERICO, V., LONGO, S., CHIAPPONI, L., ARCHETTI, R. & CIRIELLO, V. 2014 Radial gravity currents in vertically graded porous media: theory and experiments for Newtonian and power-law fluids. *Advances in Water Resources* **70**, 65–76.

GRATTON, J., MINOTTI, F. & MAHAJAN, S.M. 1999 Theory of creeping gravity currents of a non-Newtonian liquid. *Phys. Rev. E* **60(6)**, 6960–6967.

HERSCHEL, W.H. & BULKLEY, R. 1926 Konsistenzmessungen von Gummi-Benzollösungen. *Kolloid-Zeitschrift* **39** (4), 291–300.

HEWITT, D.R., DANESHI, M., BALMFORTH, N.J. & MARTINEZ, D.M. 2016 Obstructed and channelized viscoplastic flow in a Hele-Shaw cell. *J. Fluid Mech.* **790**, 173–204.

HOGG, A.J. & MATSON, G.P. 2009 Slumps of viscoplastic fluids on slopes. *Journal of Non-Newtonian Fluid Mechanics* **158**, 101–112.

HOGG, A. J, UNGARISH, M. & HUPPERT, H. E. 2000 Particle-driven gravity currents: asymptotic and box model solutions. *European Journal of Mechanics-B/Fluids* **19** (1), 139–165.

HUANG, X. & GARCIA, M.H. 1998 A Herschel-Bulkley model for mud flow down a slope. *J. Fluid Mech.* **374**, 305–333.

KING, S. E. & WOODS, A.W. 2003 Dipole solutions for viscous gravity currents: theory and experiments. *Journal of Fluid Mechanics* **483**, 91–109.

LAVROV, A. 2013 Redirection and channelization of power-law fluid flow in a rough-walled fracture. *Chem. Eng. Sci.* **99**, 81–88.

LIU, K. F. & MEI, C. C. 1989 Slow spreading of a sheet of Bingham fluid on an inclined plane. *J. Fluid Mech.* **207**, 505–529.

LONGO, S., CHIAPPONI, L. & DI FEDERICO, V. 2016 On the propagation of viscous gravity currents of non-Newtonian fluids in channels with varying cross section and inclination. *Journal of Non-Newtonian Fluid Mechanics* **235**, 95–108.

LONGO, S., CIRIELLO, V., CHIAPPONI, L. & DI FEDERICO, V. 2015*a* Combined effect of rheology and confining boundaries on spreading of porous gravity currents. *Advances in Water Resources* **79**, 140–152.

LONGO, S. & DI FEDERICO, V. 2014 Axisymmetric gravity currents within porous media: First order solution and experimental validation. *Journal of Hydrology* **519**, 238–247.

LONGO, S., DI FEDERICO, V., ARCHETTI, R., CHIAPPONI, L., CIRIELLO, V. & UNGARISH, M. 2013*a* On the axisymmetric spreading of non-Newtonian power-law gravity currents of time-dependent volume: An experimental and theoretical investigation focused on the inference of rheological parameters. *J. Non-Newton. Fluid Mech.* **201**, 69–79.

LONGO, S, DI FEDERICO, V & CHIAPPONI, L 2015*b* A dipole solution for power-law gravity currents in porous formations. *Journal of Fluid Mechanics* **778**, 534–551.

LONGO, S., DI FEDERICO, V. & CHIAPPONI, L. 2015*c* Non-Newtonian power-law gravity currents propagating in confining boundaries. *Environmental Fluid Mechanics* **15** (3), 515–535.

LONGO, S., DI FEDERICO, V. & CHIAPPONI, L. 2015*d* Propagation of viscous gravity currents inside confining boundaries: the effects of fluid rheology and channel geometry. *Proceedings of the Royal Society of London A: Mathematical, Physical and Engineering Sciences* **471** (2178).

LONGO, S., DI FEDERICO, V., CHIAPPONI, L. & ARCHETTI, R. 2013*b* Experimental verification of power-law non-Newtonian axisymmetric porous gravity currents. *J. Fluid Mech.* **731, R2**, 1–12.

LYLE, S., HUPPERT, H.E., HALLWORTH, M., BICKLE, M. & CHADWICK, A. 2005 Axisymmetric gravity currents in a porous medium. *J. Fluid Mech.* **543**, 293–302.

MAGNIN, A. & PIAU, J.M. 1987 Shear rheometry of fluids with a yield stress. *Journal of Non-Newtonian Fluid Mechanics* **23**, 91–106.

MEI, C. C. & YUHI, M. 2001 Slow flow of a Bingham fluid in a shallow channel of finite width. *J. Fluid Mech.* **431**, 135–159.

NGUYEN, Q.D. & BOGER, D.V. 1992 Measuring the flow properties of yield stress fluids. *Annual Review of Fluid Mechanics* **24** (1), 47–88.

Ostwald, W. 1929 Ueber die rechnerische darstellung des strukturgebietes der viskosität. *Colloid & Polymer Science* **47** (2), 176–187.

Pascal, J.P. & Pascal, H. 1993 Similarity solutions to gravity flows of non-Newtonian fluids through porous media. *Int. J. Non-Linear Mech* **28(2)**, 157–167.

Perazzo, C.A. & Gratton, J. 2005 Exact solutions for two-dimensional steady flows of a power-law liquid on an incline. *Phys.Fluids* **17(1)**, 013102.

Sachdev, P.L. 2000 *Self-similarity and beyond: exact solutions of nonlinear problems*. CRC Press.

Uhlherr, P.H.T., Park, K.H., Tiu, C. & Andrews, J.R.G. 1984 Yield stress from fluid behaviour on an inclined plane. In *Adv. in Rheology, MexicoCity 1984*, , vol. 2, pp. 183–190.

Vola, D., Babik, F. & Latch, J.-C. 2004 On a numerical strategy to compute gravity currents of non-Newtonian fluids. *J. Comp. Phys.* **201**, 397–420.

Wang, S. & Clarens, A. F. 2012 The effects of CO2-brine rheology on leakage processes in geologic carbon sequestration. *Water Resources Research* **48** (8).

Yasuda, K.Y., Armstrong, R.C. & Cohen, R.E. 1981 Shear flow properties of concentrated solutions of linear and star branched polystyrenes. *Rheologica Acta* **20** (2), 163–178.